NASA EPSCoR
Cooperative Agreement Number: NNX15AM77A

Advanced Transport Technologies for NASA Thermal Management/Control Systems

Technical Report
For period: July 1, 2017 to June 30, 2018

Science Principal Investigator:
Miles Greiner, Professor and Interim Chair, Mechanical Engineering Department
University of Nevada, Reno, 89557, (775) 784-4873, greiner@unr.edu

Program Director
Dr. Lynn Fenstermaker
Director of Nevada NASA EPSCoR
lynn.fenstermaker@dri.edu
Desert Research Institute
755 E. Flamingo Road
Las Vegas, NV 89119

Nevada System of Higher Education
2601 Enterprise Rd.
Reno, NV 89512
EIN: 88-6000024

Project Period: July 1, 2015 to June 30, 2018

I. Introduction

Thermal control of life-support, power electronics, and other systems is a key enabler for a variety of NASA space, air-flight, and monitoring technologies and is the topic of this research. An example system requiring advanced thermal control is the Surface Water Ocean Topography (SWOT) project, which is designed to acquire precise measurements of land hydrology and ocean circulation. The resulting data will help generate a global assessment of surface water resources and detailed ocean process mapping that will ultimately be used for climate modeling. SWOT's instruments have relatively high electronic heat-dissipation (~1 kW) and must be co-located with other components. However, the instrument temperatures must be extremely stable, with a rate of change below 0.05 K/minute. Furthermore, this must be accomplished in low-Earth orbit, where the variations of solar insolation and Earth reflectance and emission are large. To put this challenge in perspective, typical spacecraft instruments have temperature stability requirements on the order of 1 K/min, usually achieved by isolating components. Lightweight, compact, low-power and reliable thermal control technologies must be developed and proven to meet these requirements.

NASA thermal control systems typically employ liquid coolant loops that remove heat from heat-generating components and transport it to cooler modules, which either utilize the heat or reject it to space. While NASA currently relies on single-phase coolant loops (in which the liquid does not evaporate as it absorbs heat), phase-change systems (in which the coolant boils as it absorbs heat and condenses when it delivers it) can reduce the size, weight, temperature variations, and pumping power requirements of thermal control systems, without loss of reliability.

Heat pipes, loop heat pipes, and capillary pumped loops are passive phase-change thermal management systems. In each, heat is removed from high-temperature external components by the device's evaporator section (that contains a porous wick to deliver cooling liquid to surfaces where it is vaporized). The vapor is transported to a condenser section where heat is absorbed by a cooler component or rejected to space. This condenses the vapor and the resulting liquid returns to the evaporator. The capillary pressure that develops in the evaporator's wick drives the liquid and vapor flow, and no external pumping power is required.

To increase the controllability and reliability of thermal management systems, NASA is considering systems in which a pump is placed in the liquid line. Pumped two-phased loops are currently used in some military, aerospace, and electronics cooling applications. One of the objectives of the current work is to apply them to low-gravity space applications. In some terrestrial applications, as the liquid boils at a surface, the vapor is removed by buoyancy forces and replaced by fresh liquid. However, in low-gravity space environments, buoyancy is not effective. As a result, vapor can build up, insulating the surface from the liquid coolant. At a critically-high surface heat flux, this insulating layer can be sufficiently thick to cause the heated surface to fail or even melt. In pumped two-phase loops, there is some liquid flow over the heated surfaces even when buoyancy is not effective. However, little experimental or computational data exist to characterize flow boiling in low gravity environments, especially within the porous wick structures that are contained in evaporators.

II. Current UNR Work

A. Capillary Pressure Implementation in the CFD simulations

CFD simulations using ANSYS/Fluent code were carried out for a 1×1 cm^2 domain representative of a portion of the metallic porous wick used in the evaporator of the 2φMPFL system (see Fig. 1). Previous simulations (refer to the previous reports) conducted in the same domain did not take the effect of capillary pressure into consideration and the flow was solely driven by a pressure or mass flow rate applied at the inlet.
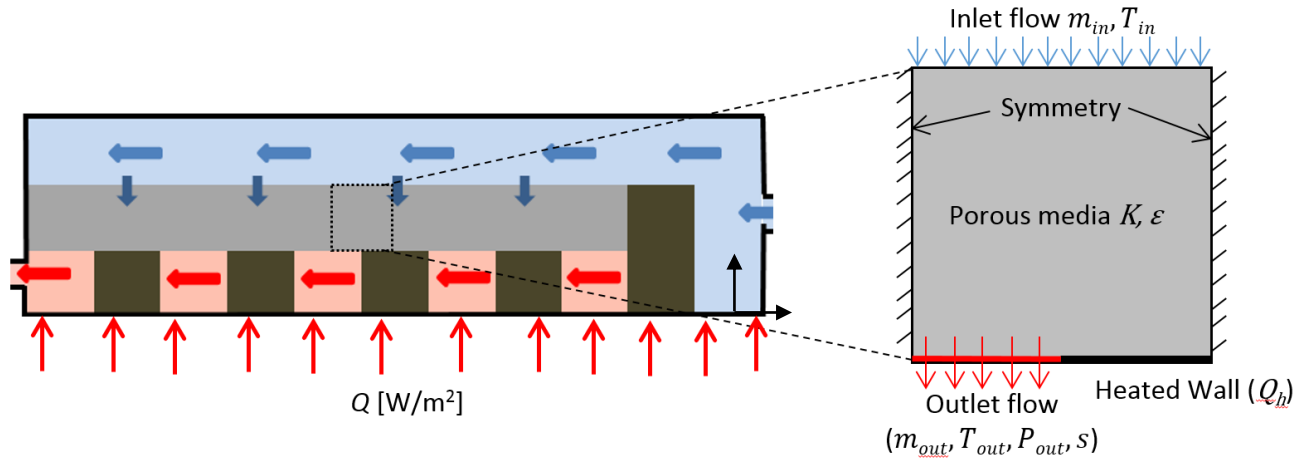
Figure 1: Schematic of the numerical model used in ANSYS/FLUENT to simulate heat transfer in a section of the evaporator wick with the boundary conditions.

The capillary pressure is an important effect on the results as it allows the vapor created at the heated surface to leave from the outlet of the domain. An attempt to include the capillary pressure in these simulations was carried out. A user-define-function written in the C programing code was created and implemented in ANSYS/Fluent. This function calculates the gradient pressure, in both x and y-direction, generated by the capillary effect and included it as a source term in the momentum equation. The capillary pressure depends on the saturation of the wetting phase. Different models for the capillary pressure were tested.

Figure 2 shows the contour of the volume fraction of water for a case with a heat input of 10 W/cm^2 and an inlet water temperature of 95°C, which is close to the saturation temperature. A gauge pressure, $P_G = 0$ Pa, was used on both inlet and outlet of the domain. The contours in these figures are shown at different times of simulation. It can be seen that, as the simulation time increases, the shape of the vapor bubble created at the heated surface changes into a rectangle. Also, small bubbles of water are created within the vapor region close to the heated surface. The researchers were not able to explain these results and concluded after many attempts that ANSYS/Fluent is not able to correctly simulate the capillary effect in porous media. Therefore, the attention was shifted to a new open source code that has a higher flexibility in term of modifying the governing equation of flow.

The open source OpenFOAM CFD code, a C++ toolbox for customized numerical solver, was used. First an attempt to simulate the capillary pressure generated in a vertical capillary tube was made. Figure 3a shows is initial conditions. The red color represents the liquid phase, while the blue color represents the gas phase. Due to the effect of capillary pressure, the level of liquid in the capillary tube should increase. In this simulation, the gravitational forces are neglected. Figure 3b and 3c show that a meniscus at the interface between the liquid and gas in created due to the surface tension effect. These figures also show that the level of liquid raised in the tube due to the capillary pressure. This result showed that OpenFOAM has the capability to model capillary flow. The next step will be to perform the simulations on the domain shown in Fig. 1.
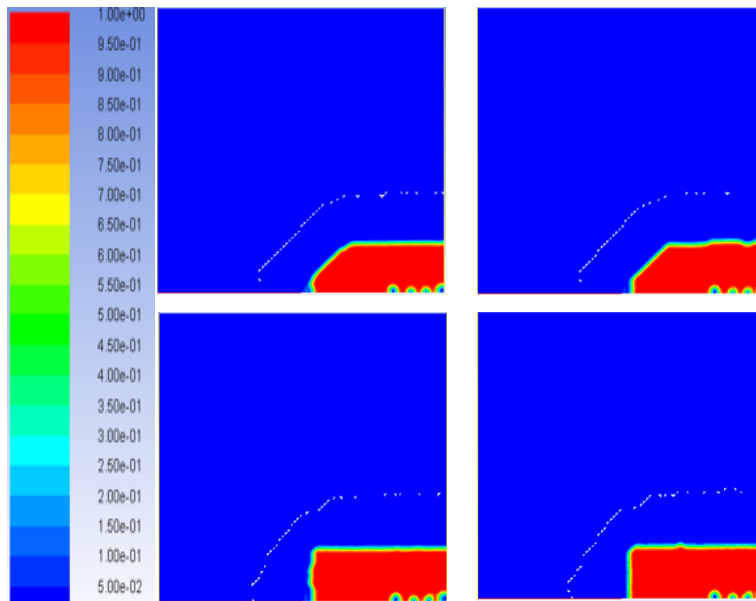
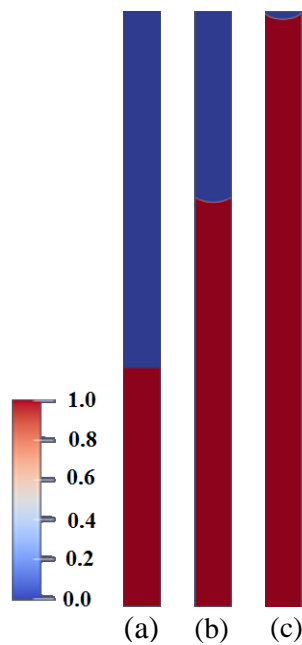Figure 2: Volume fractions contours at different time steps

(a) (b) (c)

Figure 3: Flow in a vertical capillary tube simulation in OpenFOAM

B. Two-Phase Flow and Phase-Change Experiments

An experimental setup is developed to study heat transfer and phase change in porous media. The results from this experiment will be used to benchmark the CFD simulations using OpenFOAM.

A quasi-two-dimensional experimental setup is designed and constructed. Figure 4 shows a front view of the main section of the experiment. A 1mm thick porous wick with dimensions of 10×5 cm^2 is sandwiched between two Plexiglass plates. The wick is in contact on the top surface with the stainless steel plate heated by a cartridge heater. A liquid coolant is fed to the bottom of the porous wick from a reservoir. The coolant

flows through the porous media and evaporates at the interface with the heated stainless steel plates. The resulting vapor is pushed by capillary action to the vapor chambers on both sides of the heated plates, where it accumulates and leaves through the vapor lines.
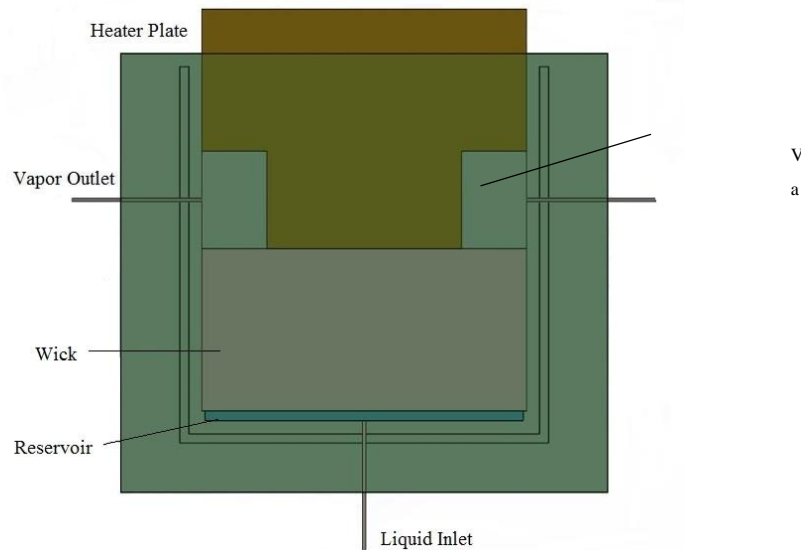

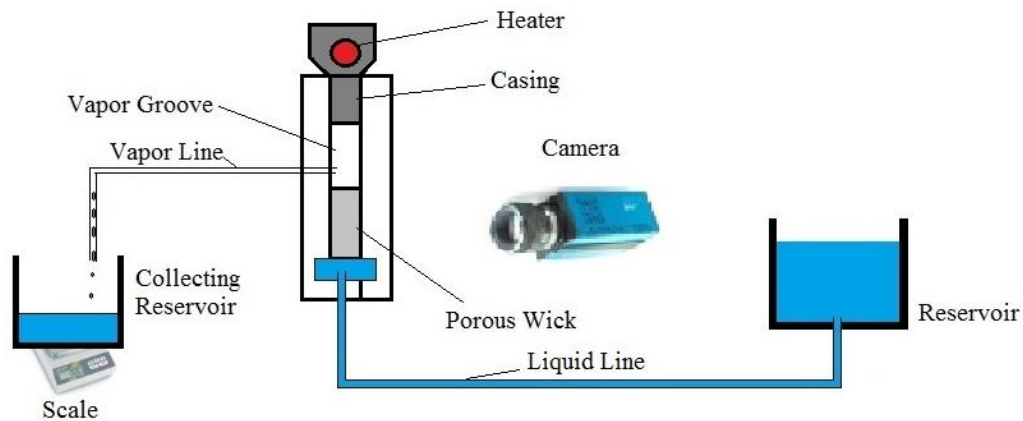Figure 4: Quasi two-dimensional experimental setup design.

Figure 5: Schematic of Overall Experimental Setup

Figure 5 shows a schematic of the experimental apparatus. A liquid reservoir is used to feed the porous wick with liquid. The level of the liquid will give the indication of the pressure at the bottom of the wick. The vapor exiting the vapor line will be condensed and the resulting liquid will be measured using a scale. Based on the mass of liquid collected, the rate of evaporation of the liquid will be calculated. Nine thermocouples are attached to the back of the stainless steel plate to calculate the heat flux going to the wick while an infrared camera is placed at the front of the experiment to take thermal images of the porous wick. A regular camera will be also used to monitor the interface of the liquid and vapor in the porous wick.

Loose Powder Sintering Method

In order to conduct the experiment described above, a porous wick is needed. Expertise in sintering porous wicks was developed by the UNR researcher. The loose powder method was used. In this method,

the metal powder is poured into a graphite mold and leveled by applying a small pressure. The mold is then put into a furnace and heated up to the sintering temperature of the metal. Figure 6 shows a cylindrical stainless steel porous wick that was fabricated using this method. A spherical powder of a size 5-20 µm was used. The sintering was done in Thermo Scientific Lindberg Box Furnace for 5 hour period at a temperature of 1000°C. Tested with water liquid were carried out to check the permeability of this porous sample. A small section of the top surface of the porous sample was scanned with a microscope to determine the morphology of the sample. The researchers are attempting to sinter 1mm thick porous media to use it in the experimental setup described above.
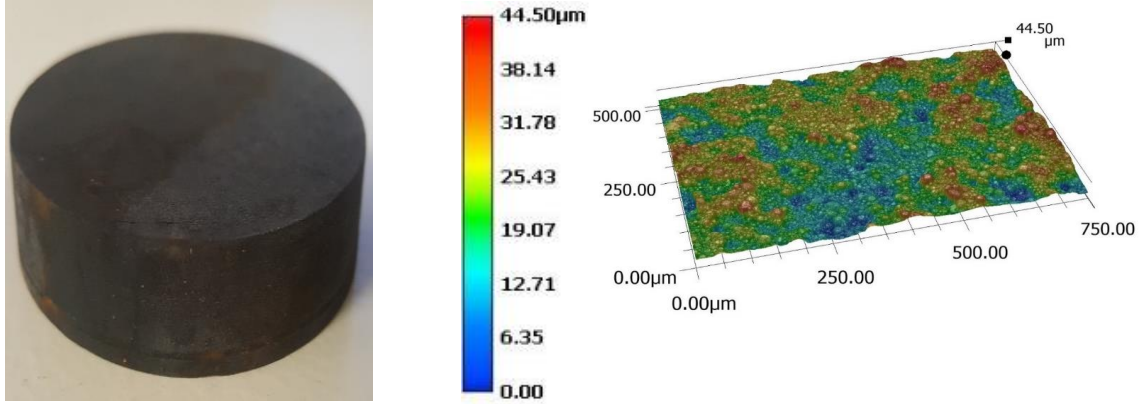

Figure 6: (a) Sintered Porous Sample and (b) Graphite Mold

III. Current UNLV Work

A. Enhanced Condensation via Surface Modification: Flow Visualization

The droplet size distribution is measured in a flat plate heat exchanger by applying a droplet detection method to images of dropwise condensation on the sample surface. The method employed in this study is a modified form of the Circle Hough Transform [1, 2]. The basic method has been modified to allow for detection of a wide range of droplet sizes. The measured droplet size distribution is used to explore time-dependent characteristics of dropwise condensation and to inform an estimate of heat flux. The measured droplet size distribution is combined with a model of individual droplet heat transfer to yield estimates of the heat flux and equivalent heat transfer coefficient. These estimates are compared with measurements of heat flux from the tube condensing heat exchanger for the same surface treatment. The droplet size distribution for droplet radii larger than the average distance between nucleation sites has been predicted by LeFevre and Rose [3]. The prediction begins with a function that defines the fraction of surface area covered by droplets of radius r and greater, and its derivative

$$f(r) = 1 - \left(\frac{r}{r_{max}}\right)^b \tag{1}$$

$$f'(r) = -\frac{b}{r}\left(\frac{r}{r_{max}}\right)^b \tag{2}$$

where r_{max} is the largest droplet size that can exist on the surface before departing due to gravity. The area fractions utilized in this theory are visualized for a sample area covered by droplets in Figure 7.
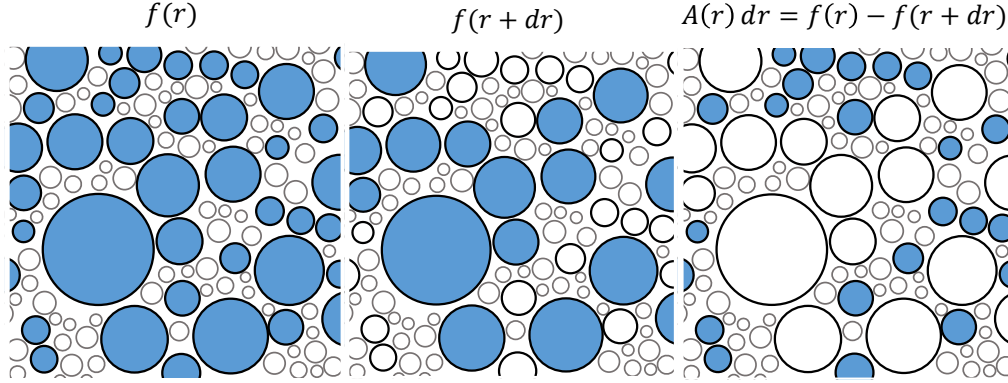
Figure 7. Representation of Area Fractions:
Left: Fractional area $f(r)$ covered by droplets with radius greater than r.
Middle: Fractional area $f(r + dr)$ covered by droplets with radius greater than $r + dr$
Right: Fractional area $A(r)\,dr$ covered by droplets with radii between r and $r + dr$.

The fraction of surface area covered by droplets greater than droplet radius r but less than droplet radius $r + dr$ is expressed in terms of Equation (2) by means of a first-order, forward Taylor series expansion of f about r

$$A(\mathrm{r})\,\mathrm{d}r = f(r) - f(r + dr) = -f'(r) \tag{3}$$

The constrained surface area fraction $A(r)$ is just the product of projected droplet area a with the number of droplets per unit area N of the condensing surface between r and $r + dr$

$$A(\mathrm{r})\,\mathrm{d}r = f(r) - f(r + dr) = -f'(r) \tag{4}$$

The projected droplet area must be specified because the radius r is defined as the radius of the spherical droplet cap, not of the circular contact area between droplet and surface. This is chosen because for contact angles greater than 90°, optical measurement of droplet radii normal to the surface yields the spherical cap radius, not the circular base radius. With the radius expressed this way, the model neglects droplets that form under the canopy of other, larger droplets. Combining Equations (2 − 4) yields LeFevre and Rose's model [3] of the droplet size distribution with a variable b index

$$N(r) = \frac{b}{\pi r^3}\left(\frac{r}{r_{max}}\right)^b \tag{5}$$

which gives the number of droplet counts expected between radii r and $r + dr$ per unit area of the condensing surface. LeFevre and Rose chose a value of 1/3 for the b index.

In this work, the sample side houses the flat plate sample, mounted to a copper plug, which is installed in the chamber and backed by a cold plate. Water from a process chiller circulates through the cold plate at 150 g/s. The copper plug is also shown in Figure 8, where the canopy is seen more clearly. The plug is placed in the apparatus such that the canopy shields the plate from condensate runoff from above. Thermal paste is applied between the sample and copper plug, as well as between the plug and cold plate, to ensure good thermal contact. The boiler flange houses a 500 cm³ internal boiler with a 250 W cartridge heater. The boiler is sized to supply steam for over an hour. An outlet on the far end of the boiler permits steam into the main chamber, where it condenses onto the sample. Auxiliary heating pads and insulation limit most of the condensation to the sample side wall. The pump side consists of a vacuum pump valve, pressure transducer and two T-type thermocouples. The sensors are used to monitor ambient conditions. The

compactness of the resulting design is convenient for visualization of condensation with a modest focal length lens. The droplet size distribution is obtained from detecting droplets on the surface over many frames of video data. Two processed frames from a video sequence are shown in Figure 9. Detections are reliable down to droplets with a four-pixel radius, corresponding to 272 μm. The number of edge pixels available for a very small droplet limits the number of votes that can be made towards its center. A lower vote threshold is set to detect such droplets. Too low a vote threshold introduces false positive detections, so a four-pixel minimum radius was chosen. Droplet sweeping events occur periodically when a droplet grows large enough to depart the surface under its own weight. The departing droplet entrains any condensate in its path. This exposes the sample surface and allows for droplets to nucleate, grow, coalesce, and eventually be swept again. The plot in Figure 10 shows sweeping events and the droplet count density over time, with the specific event from Figure 9 highlighted by a cyan-colored circle. The droplet population increases over time with growth and coalescence, but is reduced by sweeping events. The droplet size distribution emerges from this balance between droplet growth and sweeping. It gives the count density of droplets of a given radius. It is obtained by binning droplet detections in video data by their radii. Droplet counts in each bin scale with the instantaneous droplet count density shown in Figure 10. A representative droplet size distribution is obtained by averaging counts across frames of the video data.
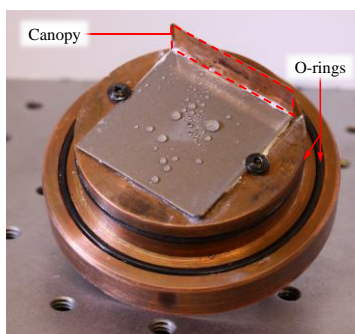

Figure 8. PC-HEX Sample Mounted to Copper Plug; The copper plug is installed in the sample side flange cap and seals with two O-rings. A canopy shields the sample from condensate runoff.
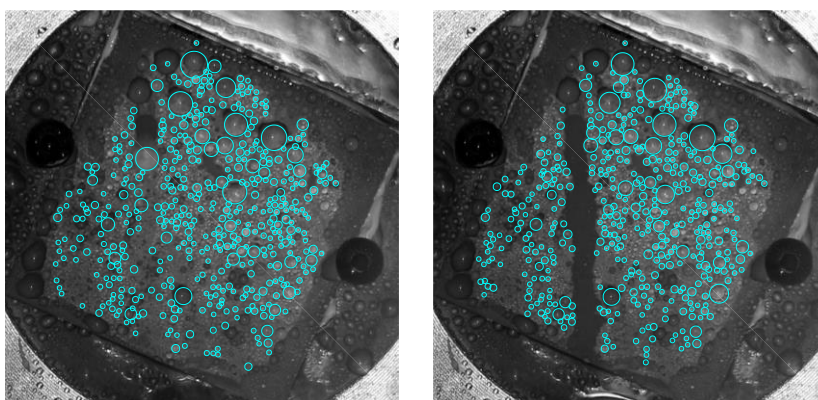

Figure 9. Processed Video Frames Highlighting Droplet Sweeping Event
Left: A processed video frame with a droplet beginning to depart the surface.
Right: A processed video frame taken 167 ms later. The droplet has swept additional condensate along with it.
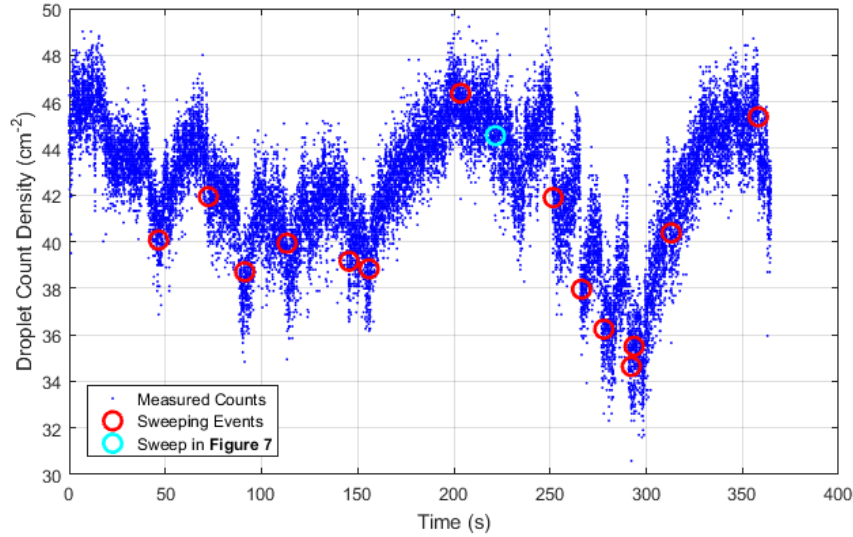
Figure 10. Droplet Count Density and Sweeping Events Over Time
Droplet nucleation causes an increase in droplet count density. Sweeping events cause a decline in the droplet count density.
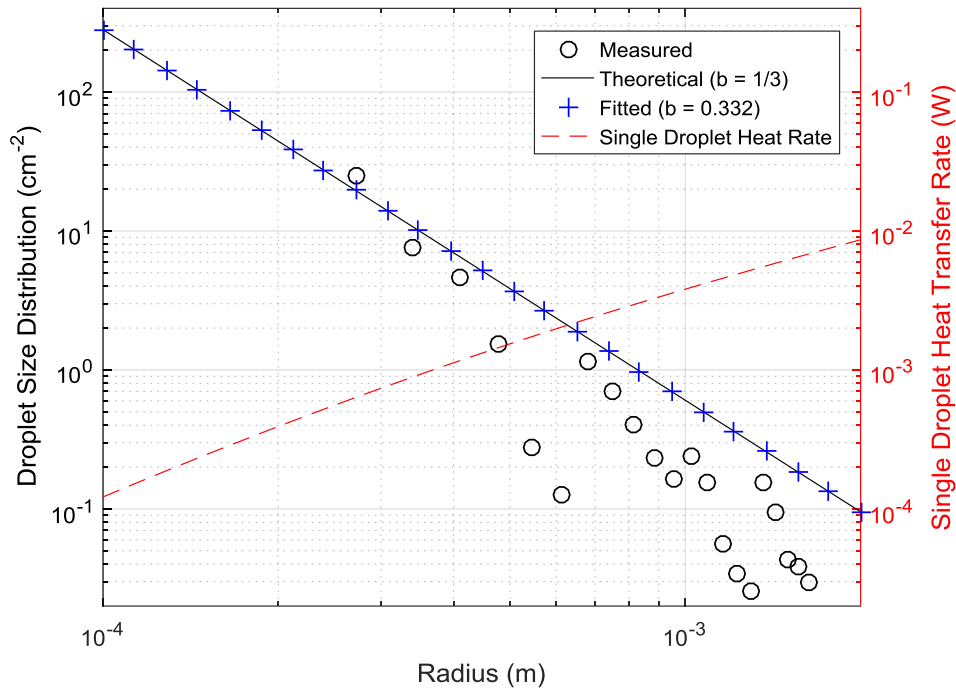

Figure 11. Droplet Size Distribution
Theoretical, fitted, and measured distributions. A bin width of 1 pixel or 68 μm is used.

This representative distribution is shown as the circular data points in Figure 11. The bin width used for binning counts is one pixel, or 68 μm. The measured distribution in is compared with the theoretical, where the b index is taken to be 1/3 from LeFevre and Rose [3]. A nonlinear least-squares fit is also made from the data to the theoretical large droplet size distribution in Equation (5) with variable b index. The fitted b index comes out to 0.3320, resulting in the fitted distribution trending very close to that with a b index

of 1/3. The leftmost circular data point in Figure 11 is the only data point above the fitted function, but it is at least one order of magnitude larger than most data points below the fitted function. Its deviation above the fitted function offsets all other points deviating below it. The active detection area of the sample is 10 cm^2, such that bins containing droplets with radii larger than 500 μm are expected to have fewer than ten droplets each. A larger sample area would permit more droplets in these bins, yielding a better estimate of the droplet size distribution. The minimum measurable droplet radius is 272 μm, while the minimum thermodynamically viable droplet radius is on the order of a nanometer. The portion of droplets from about a nanometer to 272 μm is not captured. The ability to measure the condensate droplet population is crucial in the exploration of dropwise condensation heat transfer. Results found in this study agree with the theoretical large droplet size distribution, as shown in Figure 11. A decreasing count frequency with increasing droplet radius is observed. Additionally, the experimental setup allows for observation of transient characteristics of the local droplet size distribution. An example of this type of data is presented in Figure 10. It is insightful in that it allows for tracking of the mechanisms from which the droplet size distribution emerges. Sweeping events are distinctly visible as an abrupt decline in the droplet count density. Droplets entering the measurable region by growth and coalescence result in the steady rise of the droplet count density when sweeping is not happening. These events correspond directly to real events in the video data.
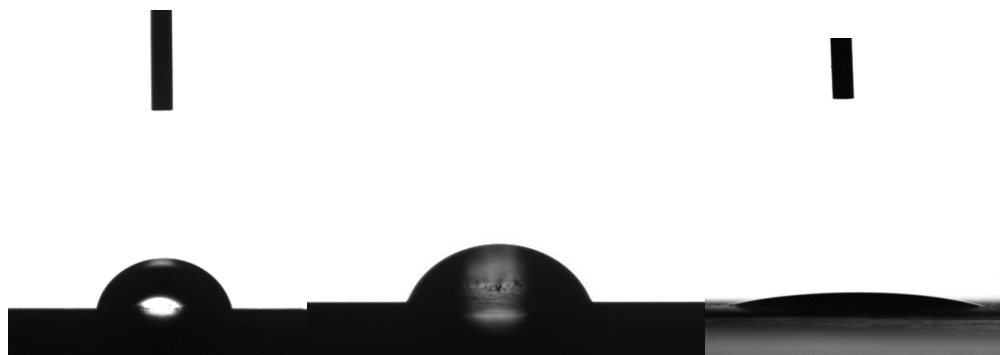

Figure 12. *Left*: Water droplet on a plain Al 6061 surface, *Middle*: Water droplet on TiO_2 coated Al 6061 with NeverWet, and *Right*: Water droplet on a TiO_2 coated Al 6061 surface

B. High performance boiling surfaces

This study focuses primarily on a passive treatment, specifically TiO_2 coating, which involves testing a substrate coated with TiO_2 using NeverWet[TM] base coating as a coupling agent and coated using a method outlined by Wu et al. [4] and comparing the overall boiling curve and heat transfer coefficient with other baseline samples for water. Anatase TiO_2 was chosen as the material for this study because it is naturally hydrophilic, and interestingly, it can become super-hydrophilic after being exposed to ultraviolet light at a wavelength of less than 380 nm. The focus, however, is on its physical properties. The local (top, bottom, and sides of the sample) boiling curve and heat transfer coefficient are also observed. The sessile drops application was used to determine the contact angles between the various surfaces. Multiple trials were conducted to find a solid average and to ensure the coating in the surfaces were even. The contact angle was found by distributing droplets throughout the sample to ensure uniformity of the surface. Figure 12 shows the droplet on a plain Al 6061 surface. The contact angle of the untreated surface was obtained to gain baseline data. The untreated Al 6061 surface averaged an 81˚ contact angle. It also shows a droplet on a TiO_2 coated Al 6061 surface that was treated with NeverWet[TM]. The contact angle on this surface averaged a 60˚ contact angle. This impact in wettability may be attributed to the base coating of NeverWet[TM].

Additionally it shows a droplet on a TiO₂ coated Al 6061 surface. It can be observed that the TiO_2 makes the surface significantly more hydrophilic. The average contact angle of the surface was 15˚.
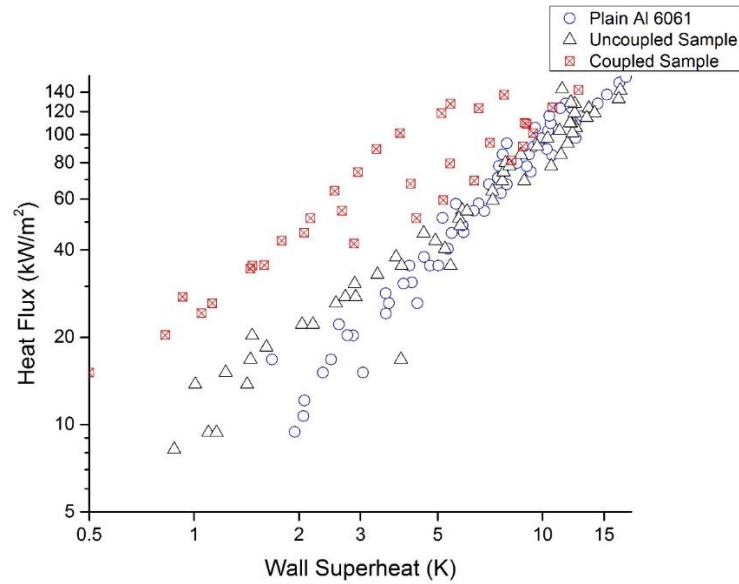

Figure 13. Pool boiling curve of baseline substrate vs both TiO_2 substrates

A pool boiling curve was generated for Al 6061 samples treated with TiO_2 with both methods. Al 6061 samples treated with NeverWet[TM] are considered the "couple sample" and the samples that were not treated with NeverWet[TM] are considered the "uncoupled sample" in Figure 13. The pool boiling curve generated from the coupled sample trends closely with the plain Al 6061 sample, whereas the uncoupled sample yields a pool boiling curve of higher performance. When looking at the wettability data for the 3 samples, the data appears convincing because the contact angle of the coupled sample and plain Al 6061 are relatively close. This is probably because of the base coating used from NeverWet[TM]. Overall, the sample that was coupled with NeverWet[TM] performance did not show much of an enhancement in boiling heat transfer, and even appears to drop off at high superheat and heat flux. The uncoupled sample has an average contact angle (15˚) that is significantly lower than the two other samples, so it appears the significant performance enhancement is probably due to the wettability and roughness of the surface of the TiO_2 coating. A hydrophilic surface with such a low contact angle should yield heat transfer enhancement through the help of bubble dynamics (faster departure frequency). This enhancement was also visually apparent with the higher bubble departure frequency and nucleation sites. Figure 14 shows images from the Phantom high-speed camera at varying heat fluxes (40, 60, and 120 kW-m⁻²). This allowed for visual observation of the differences in bubble nucleation and departure between treated and untreated surfaces of Al 6061. Comparing the left and right images of Figure 14, a clear difference can be observed between plain Al 6061 samples and treated Al 6061 samples. The difference is very clear at a low heat flux of 40 kW/m², and at 120 kW/m² the treated sample appears to have a significant amount of active nucleation sites. Overall, the Al 6061 samples that were treated with TiO_2 have significantly more nucleation points and bubble departure frequencies. From an observational standpoint, it is easy to draw a conclusion that there is more heat transfer occurring (at least through liquid-vapor exchange) with the treated samples through these images, and this can be verified by using the quantifiable information, such as active nucleation sites and bubble departure frequencies.
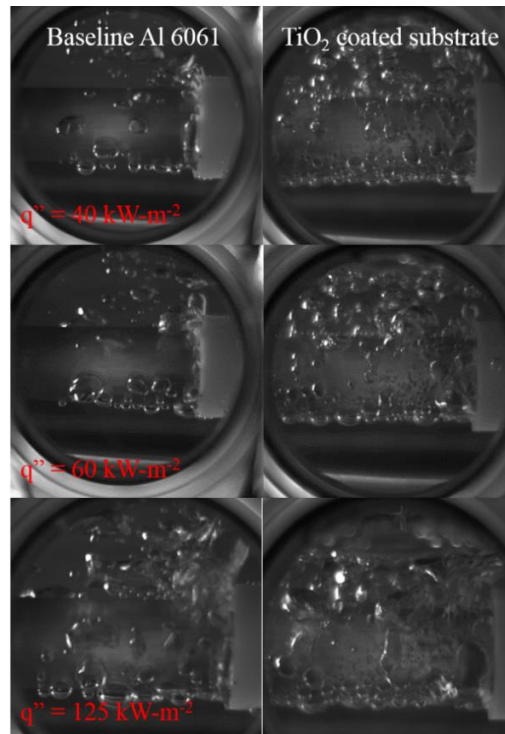
Figure 14. High speed camera images of pool boiling of baseline and TiO_2 coated sample at varying heat fluxes
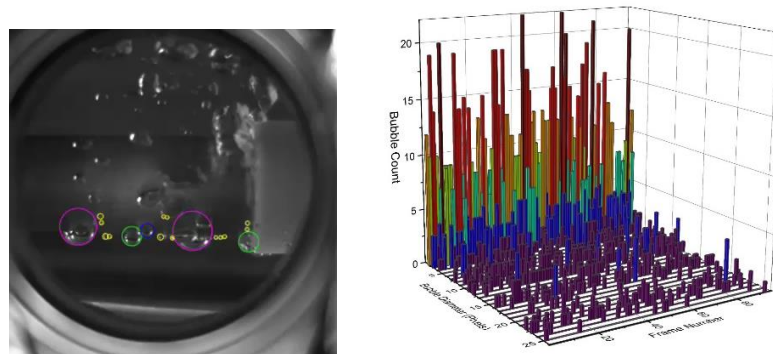

Figure 15. Image of bubble detection and Histogram of bubble count by frame

A bubble detection was conducted to analyze the videos produced by the Phantom high-speed camera. This algorithm is computationally efficient and works by plotting an arc perpendicular to the edge orientation based on the given radius. A threshold is applied to an accumulator array to detect likely centers of circles in the specified area. A .TIFF file was exported from the camera and utilized to analyze the video frame by frame. Figure 15 shows a sample image of various colored circles detecting bubbles of sizes corresponding to the color through a given area of the sample. For example, a magenta circle would be used to trace a circle between 21 and 27 pixels and a yellow pixel would be used to trace a circle between 0 and 2 pixels in radii. Using the CHT algorithm on MATLAB, bubble counts were obtained by frame. Each plot shows the bubble diameter size on the x-axis and the frame number of the video on the y-axis, and the total bubble count at the diameter and frame on the z-axis, as seen in Figure 15.

IV. Current TMCC Work

Summary of Educational Outreach Activities

Throughout the grant cycle TMCC monitored the research conducted by partners UNR and UNLV for its potential to promote research opportunities for community college students who are considering entering any engineering field. Introduction to Engineering (ENGR100) was chosen as a target because this class is the first introductory course for all engineering disciplines at UNR and TMCC. TMCC typically teaches five sections of ENGR 100 each semester. Six daytime sections were chosen to participate in a demonstration lab about the design and applications for thermal heat pipes.

A brief summary of the demographic data indicates that ENGR 100 is an excellent fit for the desired results.

- Approximately 77% of students enrolled in ENGR 100 were planning to transfer with an Associate of Science degree. The AS is the preferred TMCC degree for transfer to engineering at UNR or UNLV.
- 49% of the students are minorities
- 61% fall into the 18-24 age bracket.
- Enrollment in ENGR 100 has twice the number of students under 18 years old enrolled in ENGR 100 as the TMCC general population making this class an excellent recruitment location for future engineering students. This is due to the inclusion of the TMCC High School students in the class.
- Only 13% of engineering students at TMCC are female while the college wide average is 54%.

A PowerPoint lecture explaining the basic theory behind thermal heat pumps was scheduled for three sections taught by Co-PI Plaggemeyer during fall 2016. A demonstration lab was added in spring 2017. 145 students were enrolled in ENGR 100 in the six sections. Additional presentations are planned for April/May 2018.

Figure 16: Two ENGR 100 students comparing the thermal response rates of a copper rod and a copper

Demonstration Labs

The demonstration lab created by UNR graduate student Nishan Pandey was included during the spring semester 2017. The lab provided students a look into the current and potential applications of thermal heat

pumps. Mr. Pandey designed a demonstration unit for the lab and trained CO-PI Plaggemeyer on its operation. Co-PI Plaggemeyer then repeated the demonstration and an accompanying PowerPoint in two additional sections. It utilized findings from research conducted by UNR and UNLV. These demonstrations allowed approximately 145 community college engineering students background information on thermal heat pump applications. Figure 16 shows two students performing the demonstration lab.

Demonstration Results

Following the demonstration students were surveyed to gauge their interest in the research itself and the reaction to potential opportunities for students in their future educational endeavors. The students were asked the following questions.

	Demonstration Follow up		
	Questions	Total	%
1	**Prior to learning about the research conducted at UNR, UNLV, and TMCC**		
	I was interested in being a part of new research	31	29.5%
	I had a passing interest in participating in research at some point in the future	39	37.1%
	I had no interest in participating in a research project	33	31.4%
	No answer	2	1.9%
		105	100.0%
2	**After seeing the demonstration, I am**		
	More likely to consider research as a career	71	67.6%
	Less likely to consider research as a career	9	8.6%
	No change in my thoughts about considering research as a career	23	21.9%
	No answer	2	1.9%
		105	100.0%

The survey was not mandatory. 105 students out of 145 students responded for a 72% response rate. Approximately 30 % were already interested in research while 31% had no interest in research. That interest level increased to almost 68% indicating that the demonstration and presentation had moved some of the students from have no interest or a passing interest into the more likely to consider research as a career category.

References

[1]   T.J. Atherton, D.J. Kerbyson, Size invariant circle detection, Image Vis. Comput. 17 (1999) 795–803.

[2]   E.R. Davies, Computer and machine vision: theory, algorithms, practicalities, Academic Press, 2012.

[3]   E.J. LeFevre, J.W. Rose, A theory of heat transfer by dropwise condensation, in: Chem. Eng. Prog., AMER INST CHEMICAL ENGINEERS 345 E 47TH ST, NEW YORK, NY 10017, 1966: p. 86.

[4]   Wu, W., Bostanci, H., Chow, L. C., Hong, Y., Su, M., & Kizito, J. P. (2010). Nucleate boiling heat transfer enhancement for water and FC-72 on titanium oxide and silicon oxide surfaces. International Journal of Heat and Mass Transfer. https://doi.org/10.1016/j.ijheatmasstransfer.2010.01.013.